This document is the accepted manuscript version of the following article:
Jordan, I., Huppert, M., Rattenbacher, D., Peper, M., Jelovina, D., Perry, C., … Wörner, J. (2020). Attosecond spectroscopy of liquid water. Science, 369(6506), 974-979. https://doi.org/10.1126/science.abb0979

Attosecond spectroscopy of liquid water

Inga Jordan, Martin Huppert[†], Dominik Rattenbacher[‡], Michael Peper, Denis Jelovina, Conaill Perry, Aaron von Conta, Axel Schild, and Hans Jakob Wörner[*]

Laboratorium für Physikalische Chemie, ETH Zürich, Zurich, Switzerland

[*]Corresponding author: hwoerner@ethz.ch; www.atto.ethz.ch.

[†]Present address: Paul Scherrer Institut, CH-5232 Villigen PSI, Switzerland

[‡]Present address: Max Planck Institute for the Science of Light, Staudtstr. 2, D-91058 Erlangen, Germany

Electronic dynamics in liquids are of fundamental importance, but time-resolved experiments have so far remained limited to the femtosecond time scale. Here, we report the extension of attosecond spectroscopy to the liquid phase. We measure time delays of 50-70 attoseconds between the photoemission from liquid and gaseous water at photon energies of 21.7-31.0 eV. These photoemission delays can be decomposed into a photoionization delay sensitive to the local environment and a delay originating from electron transport. In our experiments the latter contribution is shown to be negligible. By referencing liquid to gaseous water, we isolate the effect of solvation on the attosecond photoionization dynamics of water molecules. Our methods define an approach to separating bound and unbound electron dynamics from the structural response of the solvent.

Owing to its importance for life, the study of liquid water has been at the heart of physical sciences since their emergence. Although undoubtedly being the most studied liquid, the properties of water are still far from being understood. Water displays over 70 anomalies in its physical properties (1–3). Even the structure of liquid water with its rapidly fluctuating hydrogen-bond network remains an object of intense debates (4–7). The wide range of open questions associated with liquid water and their far-reaching implications explain the considerable attention that it has always attracted. Most novel experimental techniques have therefore been applied to its study, ranging from nuclear magnetic resonance (8) to infrared spectroscopy (9), to X-ray spectroscopies (10) and to X-ray scattering (11).

In spite of these considerable efforts, many properties of liquid water remain mysterious. This fact is partially the consequence of a mismatch between the temporal resolution of the available techniques and the ultrafast dynamics of liquid water. A prominent example is the observation of a splitting in the X-ray emission spectrum of the outermost-valence band of liquid water, which is assigned either to two structural motifs of liquid water, differing in the hydrogen-bond structure (12), or to dynamics in the core-hole state (13). Differentiation of these two interpretations would require sub-femtosecond temporal resolution. Hence, probing liquid water on ever shorter time scales may allow for a better understanding of at least some of its unusual properties.

In this work, we applied attosecond spectroscopy to study liquid water. Whereas isolated molecules of increasing complexity have been studied with attosecond temporal resolution (14–17), a deeper understanding of electronic dynamics in real chemical and biological processes requires an extension of attosecond science to the liquid phase. As the main distinguishing feature compared to most femtosecond spectroscopies, the inherent time scale of the present measurements freezes all types of structural dynamics, leaving only the fastest electronic dynamics as possible contributions.

Here, we concentrated on the measurements of time delays in photoemission. Previous measurements on atoms (18, 19) and molecules (17, 20), with supporting theoretical work (21–23), established that such experiments access photoionization delays caused by the propagation of the photoelectron through the potential created by the parent ion. Similar measurements on metals (24–26) revealed the dominant influence of the electron transport time from the point of

ionization to the surface. The additional role of initial-state and final-state effects was highlighted in Refs. (27–29). Recent work on nanoparticles (30) interpreted the time delays as being dominantly sensitive to inelastic scattering times on the basis of purely classical simulations that neglected the time delays due to photoionization and scattering. Here, we developed a model that describes such time delays on a fully quantum-mechanical level and combined it with a semi-classical trajectory Monte-Carlo simulation of electron transport, which includes elastic and inelastic electron scattering, the quantum-mechanical phase accumulated along all possible electron trajectories, as well as the resulting interference effects. We showed that, in general, the measured time delays encode both scattering delays and mean-free paths, in addition to the photoemission delay.

The concept of our measurement is illustrated in Fig. 1. We used attosecond interferometry to measure the time delay between the photoemission from water in its liquid and gaseous forms. Liquid water was introduced into a vacuum chamber through a $\sim$25 μm inner-diameter quartz

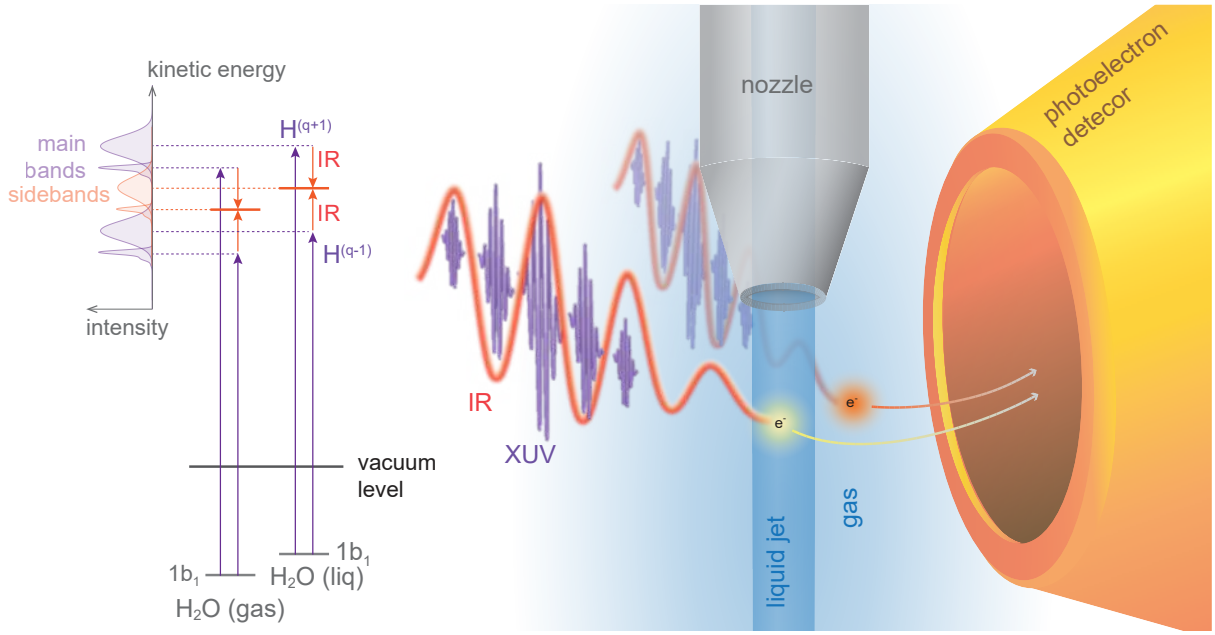

Figure 1: **Attosecond time-resolved photoelectron spectroscopy of liquid water**. A spectrally filtered attosecond pulse train, composed of a few high-harmonic orders (such as $H^{(q-1)}$,$H^{(q+1)}$, etc.) superimposed with a near-infrared (IR) femtosecond laser pulse interacts with a microjet of liquid water. Photoelectrons are simultaneously emitted from the liquid and the surrounding gas phase (see inset). The resulting photoelectron spectra are measured as a function of the time delay between the overlapping pulses.

nozzle. Evaporation from the jet created the surrounding gas phase. An extreme-ultraviolet (XUV) attosecond pulse train (APT) obtained through high-harmonic generation of a $\sim$30 fs near-infrared (IR) laser pulse in an argon gas cell, together with a strongly attenuated replica of the IR laser pulse were focused onto the liquid microjet with a spot size of $\sim$50 μm, resulting in the detection of electrons from both phases simultaneously. More details of the experimental setup are given in the Supplementary Material (SM).

The photoelectron signals from the liquid phase are shifted and broadened compared to the gas-phase signals, as schematically illustrated in Fig. 1, which enabled their discrimination. Photoemission induced by the APT created several replica of the photoelectron spectra (shown in blue in Fig. 1). The simultaneous presence of the APT and IR pulses resulted in the formation of side-band spectra, shown in red in Fig. 1. Because these sidebands (SB) can be created through two different quantum pathways, their intensity oscillates as a function of the delay between the APT and IR pulses.

A general challenge in attosecond time-resolved measurements originates from the spectral bandwidth of attosecond pulses. The resulting spectral congestion is considerably reduced by using an APT (17, 31). Nevertheless, most complex systems usually have broad photoelectron spectra, which makes the application of attosecond photoelectron spectroscopy difficult. This challenge has been addressed by using metallic filters to reduce the spectral overlap (17, 19) and additionally performing an energy-dependent analysis of the side-band oscillation phases (31, 32). In the general case of broad overlapping photoelectron spectra, these approaches are no longer sufficient. We therefore combined these ideas with a general approach, the complex-valued principle-component analysis (CVPCA) that has been numerically validated in (33).

Figure 2 shows the experimental results obtained with APTs transmitted through Sn or Ti filters, respectively, resulting in a spectral restriction to harmonic orders 11, 13 and 15 (Sn), or 17, 19 and 21 (Ti). Panels a of Fig. 2 show the photoelectron spectra recorded in the absence (blue circles) or presence (orange circles) of the IR field and panels b show the difference spectrum (”IR on” - ”IR off”, black circles) recorded on a single-shot basis by chopping the IR beam at half of the laser repetition rate. The spectra are dominated by the photoelectrons originating from the highest valence band of liquid water (light blue), the highest occupied molecular orbital of isolated water molecules (dark blue), as well as the respective sidebands

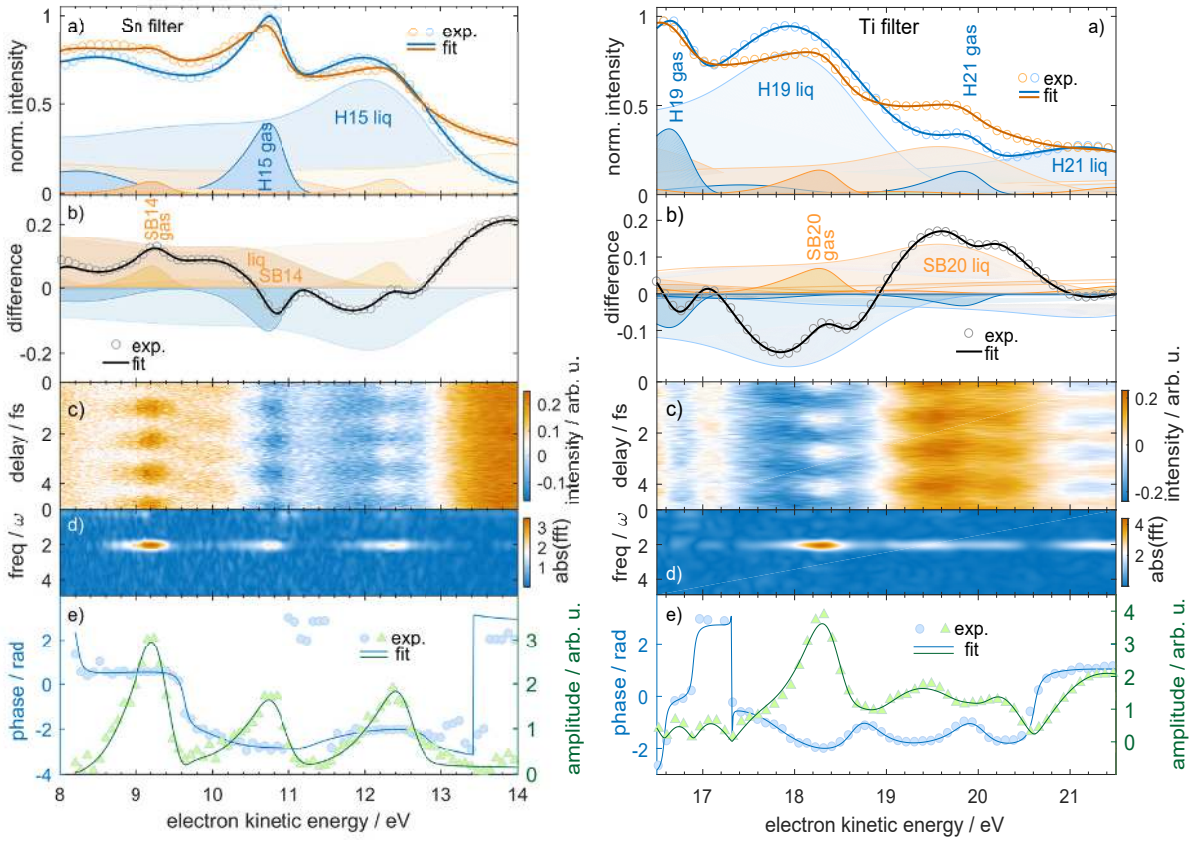

Figure 2: **Attosecond photoelectron spectra of liquid and gaseous water**. Data acquired with a Sn-filtered APT (left) or a Ti-filtered APT (right). a) Photoelectron spectra in the absence (blue) and presence (orange) of the IR field with their principal-component fit (full lines) and decomposition (filled curves). b) Difference spectra (circles), principle-component fit (line) and decomposition (filled curves) into side bands (orange) and depletion (blue). c) Difference spectra as a function of the APT-IR time delay. d) Fourier-transform power spectrum of c. e) Amplitude and phase of the 2ω component of the Fourier transform.

(light and dark orange, respectively).

In order to achieve the highest accuracy, we based the analysis on principal-component spectra that were measured with the same liquid-microjet photoelectron spectrometer (34), but replacing the APT with isolated high-order harmonics selected in a time-preserving monochromator (35). The corresponding photoelectron spectra obtained with harmonics 11 to 21 are shown in the SM (Fig. S1). These principal components were used to decompose the photoelectron and difference spectra in Fig. 2 into the individual contributions of the high-harmonic orders and the two phases of water. Positive contributions in the difference spectra (panels b) represent side bands, whereas the negative contributions originate from the depletion of the main

photoelectron bands.

Panels c of Fig. 2 show the difference spectra as a function of the APT-IR delay. Distinct oscillations with a period of 1.33 fs can be observed in both spectrograms in the spectral regions corresponding to, both, gas- and liquid-phase contributions. Panels d show the power spectrum of the Fourier transform of panels c. They reveal the presence of the expected 2ω oscillations (where ω is the angular frequency of the IR laser).

Panels e of Fig. 2 show the complex-valued Fourier-transform of panels c, obtained by integration over the width of the 2ω peak. Importantly, the phases (blue circles in panels e) are not flat, but vary across most energy ranges, as do the amplitudes (green triangles). We find that our CVPCA fully reproduces the complex-valued Fourier transform by attributing a unique phase shift and modulation depth to each of the principal components. Details on this procedure are given in the SM (Section 2.3).

This analysis reliably provides the time delays between photoemission from the liquid and gas phases as $\Delta\tau = \tau_{\mathrm{liq}} - \tau_{\mathrm{gas}} = (\phi_{\mathrm{liq}} - \phi_{\mathrm{gas}})\,/(2\omega)$. We obtain $\Delta\tau = 69 \pm 20$ as in the case of side band 14 (21.7 eV photon energy) and $\Delta\tau = 49 \pm 16$ as in the case of side band 20 (31.0 eV photon energy). The statistical analyses leasing to these results are given in Table S1 and Figs. S4 and S5 (SM). The positive sign of the relative delays indicates that the electrons from liquid water appear to be emitted later than those from water vapor.

The second observable is the modulation depth M, where $M = 1$ signifies a perfect contrast of the side-band oscillation. In the gas phase, values of $M \geq 0.95$ are usually observed (see, e.g., Figs. 1 and 2 of Ref. (17) for an experiment using the same apparatus and nearly identical experimental conditions). In the gas phase, deviations of M from unity are caused by the incoherent superposition of oscillations with different phase shifts, experimental imperfections, or small differences in the amplitudes of the two quantum paths leading to the same side-band state. Here, we concentrate on the analysis of the relative modulation depths between the liquid- and gas-phase signals, which eliminates the latter two effects. The relative modulation depths $M_{\mathrm{r}} = M_{\mathrm{liq}}/M_{\mathrm{gas}}$ amount to 0.17 ± 0.03 and 0.45 ± 0.06 in the case of side bands 14 and 20, respectively.

We first discuss the role of the near-field distributions around the liquid microjet, which have been calculated with finite-element time-dependent methods (see Figs. S6 and S7). The

near-field distributions make a negligible contribution to the delay of $\tau_{\mathrm{liq}} - \tau_{\mathrm{gas}} = -5$ as. They moreover cause a reduction of the modulation contrast of 3% for the liquid phase and 6% for the gas phase. Importantly, both effects are opposite in trend to the measured results and much smaller in magnitude.

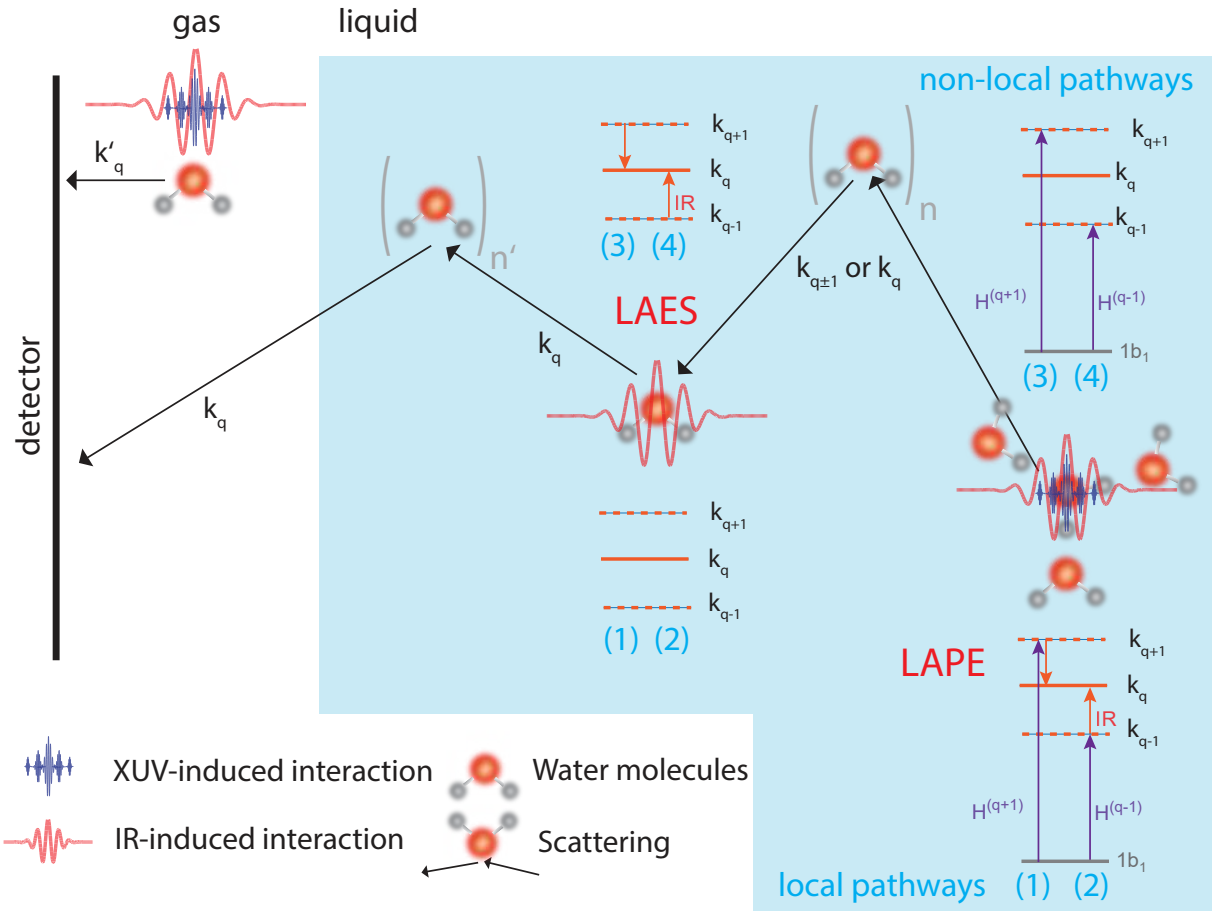

Figure 3: **Physical mechanisms of attosecond interferometry in liquid water**. In the gas phase, the XUV- and IR-induced interactions are both localized to the same molecule. In the condensed phase, we distinguish "local" pathways ((1) and (2)), followed by additional scattering events without exchange of photons, and "non-local" pathways ((3) and (4)), consisting of ionization, followed by one laser-assisted scattering event (incl. exchange of one photon with the IR field) among $n + n'$ non-laser-assisted collisions. Along the local pathways, photoelectron wave packets with central momenta k_q are launched. The non-local pathways correspond to the launch of wavepackets with central momenta k_{q-1} and k_{q+1} that are converted to a central momentum k_q through a remote LAES interaction.

Attosecond interferometry in liquids can be understood as a fully coherent combination of photoionization and electron scattering during transport to the surface of the jet (Fig. 3). Our

previous analysis (36) has shown that such experiments can be rationalized by combining the laser-assisted photoelectric effect (LAPE) with laser-assisted electron scattering (LAES). We distinguish "local" pathways, when the XUV and IR fields act at the same location in space, and "non-local" pathways where the XUV interaction (photoionization) and IR interaction (LAES) take place at different spatial positions.

For clarity we first discuss the one-dimensional case, modelling photoionization with an attractive potential and electron-water scattering with a shallower repulsive potential (Fig. 4). For sufficiently high photon energies, a single collision results in a total delay that oscillates between $\tau^{\mathrm{PI}} + \tau^{\mathrm{sca}}$ and $\tau^{\mathrm{PI}} - \tau^{\mathrm{sca}}$, where τ^{PI} and τ^{sca} are the Wigner delays for photoionization and scattering, respectively, as a function of the distance between the locations of LAPE and LAES with a spatial period $L = 4\pi/(k_{q+1} - k_{q-1})$ as shown in Fig. 4b. This oscillation is caused by the interference between local and non-local pathways along which the photoelectron wave packets have accumulated different amounts of phase because of their different central momenta (k_{q-1}, k_q or k_{q+1}). In the presence of an exponential distribution of path lengths, corresponding to a given elastic mean-free path (EMFP), the observed delay monotonically decays from $\tau^{\mathrm{PI}} + \tau^{\mathrm{sca}}$ to τ^{PI} (36). In the case of n = IMFP/EMFP elastic collisions, where IMFP stands for the inelastic mean-free path, the total delay decays from $\tau^{\mathrm{PI}} + n\tau^{\mathrm{sca}}$ to τ^{PI} about n times faster (Fig. 4c).

We hence draw the (general) conclusion that in the limit EMFP$\ll L/n$ (or IMFP$\ll L$), the classical limit is reached and the total delay is simply the sum of the photoionization and all scattering delays. In the opposite limit (EMFP$\gg L/n$, i.e. IMFP$\gg L$) the effect of the scattering delays cancel, such that the total delay becomes equal to the photoionization delay.

The MFPs of slow (≤ 50 eV) electrons in liquid water are extremely difficult to calculate and no reliable experimental measurements exist, as summarized in (37). Therefore, we developed an approach to determine the elastic and inelastic MFPs based on first-principles electron-molecule scattering calculations to determine the differential scattering cross section (DCS) for electron scattering with liquid water (38). These DCS are used in a trajectory Monte-Carlo simulation to uniquely determine the unknown EMFP and IMFP, required to describe electron scattering event by event, from the two recent experimental measurements (39, 40). Details of this procedure are given in Ref. (38). The relevant EMFPs (IMFPs) amount to 0.56 nm (3.8 nm)

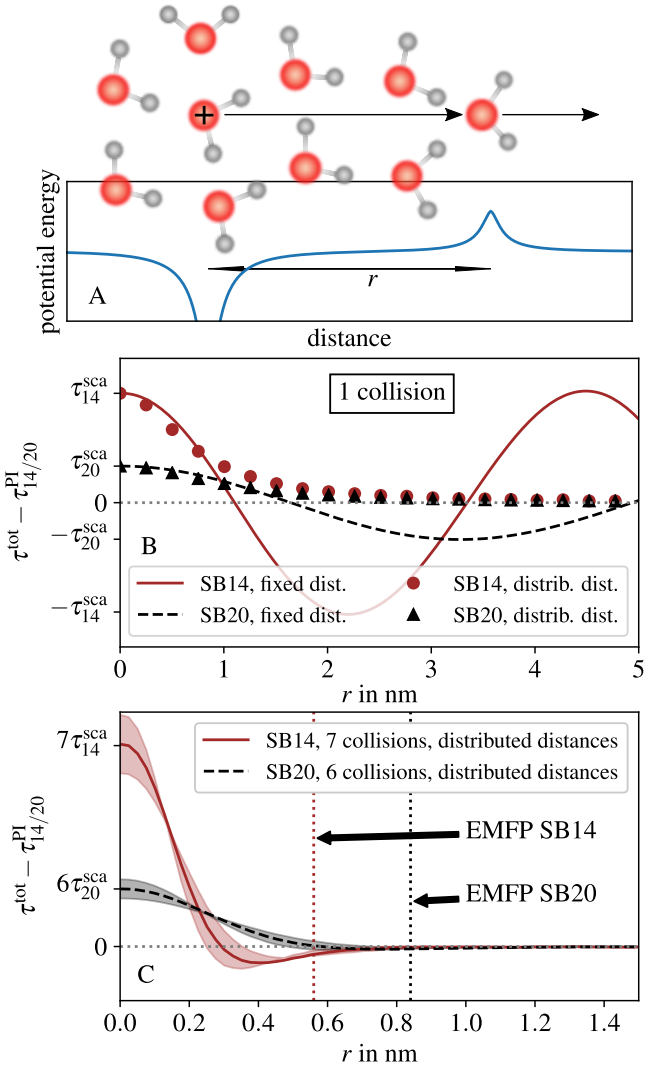

Figure 4: **Contributions of photoionization and scattering to the measured delays**. A, Schematic representation of the potentials used in the TDSE calculations, B, total delays (τ_{tot}) for the case of a single collision at a fixed distance (lines) and an exponential path-length distribution with average r (symbols), C, case of n elastic collisions, sampled according to an exponential path-length distribution with average r. The shaded areas represent one standard deviation of the corresponding MFPs.

and 0.84 nm (4.6 nm) for the two kinetic energies corresponding to SB14 and SB20, respectively. These MFPs are thus sufficiently large to cancel the scattering contributions to the total delays (Fig. 4c).

We further verified this conclusion through a complete three-dimensional calculation, which is described in Section 5 of the SM and implements all physical mechanisms shown in Fig.

3. Our model is based on semi-classical Monte-Carlo trajectory calculations, but includes the phases and amplitudes derived from a quantum-mechanical treatment of photoionization, electron scattering, LAPE, LAES and transport in three dimensions, which were derived from our earlier one-dimensional model (36). The Monte-Carlo trajectory calculations rely on accurate complex-valued scattering factors obtained from ab-initio scattering calculations of electrons with water clusters, for which convergence of the DCS has been observed with increasing cluster size and they use the associated values of the EMFP and IMFP (38). More than 10^8 classical trajectories were launched from at least 10^3 randomly selected initial positions with a momentum of either k_{q-1} or k_{q+1} (where $q = 14$ or 20 are realized in different sets of calculations). The results of these calculations are given in Fig. S11. The contribution of electron scattering during transport amounts to 0 to 6 attoseconds, depending on the depth from which the electrons originate, which averages to $\sim$2 attoseconds over all probed depths. Hence, these contributions are negligible in comparison with the measured delays of $\sim$50-70 as.

Having excluded the contributions from electron scattering and the near-field distributions, we now turn to the photoionization delays. Figure 5 shows the calculated photoionization delays of the isolated water molecule, a water pentamer, corresponding to one complete solvation shell and a $(H_2O)_{11}$ cluster, which possesses a partial second solvation shell. Details are given in Section 6 of the SM. A tetrahedral coordination of each water molecule with an O-O distance of 2.75 Å, corresponding to the structure of liquid water, was chosen. The delays systematically increase with the addition of solvation shells. The increase of the delay from H_2O to $(H_2O)_{11}$ amounts to 61 as at 21.7 eV and 30 as at 31.0 eV. These numbers compare well with the experimentally measured relative delays of 69$\pm$20 as and 49$\pm$16 as (red box in Fig. 5), particularly when noticing the slower convergence of the delay with cluster size at the higher photon energy.

Because the solvation structure of liquid water is an important and still controversial topic (see, e.g., Ref. (4–7)), we studied the sensitivity of the delays to local structural distortions. Using the most representative solvation structures identified in X-ray absorption spectroscopy (4, 12), we stretched one O-O distance in the water pentamer from 2.75 Å to 3.50 Å (blue arrow in Fig. 5) or rotated one water molecule by 50° around the central molecule. In the case of $(H_2O)_{11}$, the same operations were applied to one group of three water molecules attached to the central one. Our measured delays are consistent with both the unperturbed tetrahedral coordina-

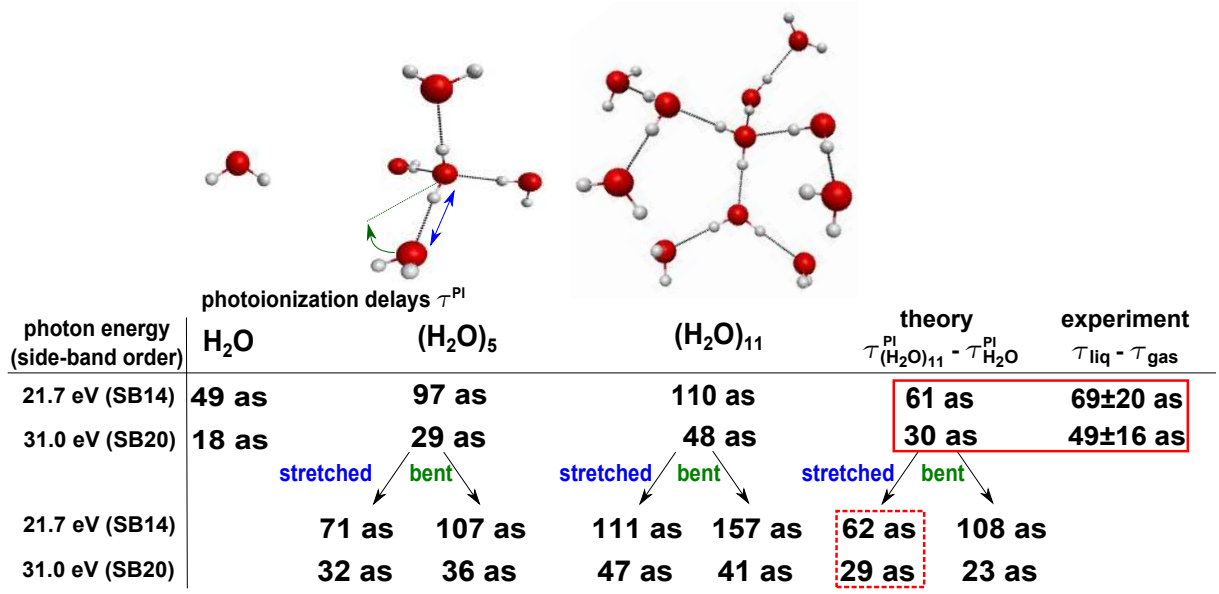

Figure 5: **Effect of the local solvation structure on photoionization delays**. Calculated photoionization delays for H_2O, $(H_2O)_5$ and $(H_2O)_{11}$. The bottom two rows indicate delays obtained by stretching (blue arrow) or bending (green arrow) one hydrogen bond in the clusters. $(H_2O)_{11}$ was the largest entity for which fully converged delay calculations were possible with a typical computational cost of 180 CPU days per calculation.

tion (see red box in Fig. 5) and with a single hydrogen bond being broken by stretching (dashed red box), but not by bending. Photoionization delays therefore discriminate between stretched or bent solvation structures, which yield indistinguishable X-ray absorption spectra (curves c and e of Fig. 3A in (4)). Our measurements are thus consistent with a dominantly tetrahedral coordination of liquid water, they do not exclude the contribution of stretched hydrogen bonds, but they do exclude a dominant fraction of hydrogen bonds being broken by bending. These sensitivities moreover motivate the application of attosecond interferometry to ice and supercooled water, which are structurally more or less homogeneous than liquid water, respectively.

We now return to the interpretation of the reduced modulation depths observed for the liquid phase. Based on Fig. 5, these finite contrasts most likely originate from a distribution of local solvation structures, which results in a distribution of photoionization delays. The superposition of interferometric oscillations with a distribution of phase shifts will indeed result in a reduced contrast of the interferometric oscillation. The larger sensitivity of the delays calculated at 21.7 eV (ranging from 110-157 as) compared to 31.0 eV (41-48 as) is consistent with the lower

relative modulation depth of 0.17 ± 0.03 and 0.45 ± 0.06, respectively. An additional possible contribution to the reduced contrast comes from decoherence of electrons in liquid water. In the case of the non-local pathways (see Fig. 3), the collisions taking place between photoionization and LAES can cause decoherence of the propagating electron wavepacket, which would also result in a reduced modulation contrast. Non-local attosecond interferometry therefore offers a possible approach to measuring the loss of electronic phase coherence during electron transport in matter.

The time delays determined in our work reflect the effect of the solvation environment on i) the electronic structure of water molecules and ii) the multiple scattering of the outgoing photoelectron. This assignment is confirmed by the dominant influence of the first two solvation shells (i and ii) and the decrease of the solvation-induced delays with the kinetic energy (ii). The measurement of photoemission time delays from liquids can thus be viewed as an attosecond time-resolved, fully coherent, electron scattering experiment from within. Compared to diffraction techniques based on external sources, it has the advantage of selectively probing the immediate environment of the ionized species. Compared to X-ray spectroscopy it offers a temporal resolution reaching down to a few attoseconds. These aspects open new perspectives in solvation science, such as the measurement of the purely electronic solvent response following electronic excitation, relaxation or large-amplitude chemical dynamics. They additionally offer the perspective of time resolving both local and non-local electronic relaxations in the liquid phase, such as Auger decay, intermolecular Coulombic decay (41, 42) and electron-transfer-mediated decay (43).

In conclusion, we have reported the extension of attosecond spectroscopy to the liquid phase. Photoemission from the most weakly bound valence band of liquid water is delayed by 50-70 attoseconds compared to the photoemission from the HOMO of the isolated molecule. Detailed calculations indicate that the contributions of electron transport to the measured delays are negligible and identify solvation as the main contribution to the measured delays. The measured delays are dominated by the first two solvation shells of water and are sensitive to the local solvation structure. Although demonstrated on practically pure liquid water, our techniques are directly applicable to other liquids and solutions, thereby establishing the applicability of attosecond spectroscopy to solvated species. This development has the potential of

expanding attosecond science into the realms of chemistry, material science and biology.

Acknowledgments

We thank Andreas Schneider, Markus Kerellaj and Andres Laso for technical support, Thomas Gaumnitz for help with the operation of the laser system, Arohi Jain for preliminary calculations of photoionization delays, Jeremy Richardson and Zhong Yin for discussions. We thank Thomas Fennel and Lennart Seiffert for their contributions to the near-field calculations and their initial support with the 1D calculations presented in this work. **Funding** We gratefully acknowledge funding from an ERC Starting Grant (Project No. 307270-ATTOSCOPE), an ERC Consolidator Grant (Project No. 772797-ATTOLIQ) and the NCCR-MUST, a funding instrument of the Swiss National Science Foundation. A. S. is grateful for support by an Ambizione grant of the Swiss National Science Foundation. D.J. acknowledges the FP-RESOMUS fellowship program. Results have been partially calculated on the NCCR-Cluster supercomputer. **Author Contributions** I.J. and M.H. built the experimental setup and performed the measurements. I.J. analyzed the data. A.C. contributed to the measurements of the monochromatic photoelectron spectra. D.R., M.P., I.J. and C.P. contributed to the development of the theoretical model and calculations. A.S. performed the Monte-Carlo trajectory simulations. D. J. realized the photoionization-delay calculations. H.J.W. supervised the project and wrote the manuscript with input from all co-authors. **Competing Interests** None to declare **Data Availability Statement** All data needed to evaluate the conclusions in the paper are present in the paper or the supplementary materials, as well as online at Zenodo (44).

Supplementary Materials

Materials and Methods

Figs. S1 to S12

Tables S1 to S2

References (45-58)

References and Notes

1. F. H. Stillinger, *Science* **209**, 451 (1980).

2. J. R. Errington, P. G. Debenedetti, *Nature* **409**, 318 (2001).

3. A. Nilsson, L. G. Pettersson, *Nature communications* **6**, 8998 (2015).

4. P. Wernet, *et al.*, *Science* **304**, 995 (2004).

5. J. D. Smith, *et al.*, *Science* **306**, 851 (2004).

6. G. N. I. Clark, G. L. Hura, J. Teixeira, A. K. Soper, T. Head-Gordon, *Proceedings of the National Academy of Sciences* **107**, 14003 (2010).

7. K. Yamazoe, J. Miyawaki, H. Niwa, A. Nilsson, Y. Harada, *The Journal of chemical physics* **150**, 204201 (2019).

8. J. Ropp, C. Lawrence, T. Farrar, J. Skinner, *Journal of the American Chemical Society* **123**, 8047 (2001).

9. H. Bakker, J. Skinner, *Chemical reviews* **110**, 1498 (2009).

10. T. Fransson, *et al.*, *Chem. Rev.* **116**, 7551 (2016).

11. T. Head-Gordon, G. Hura, *Chemical reviews* **102**, 2651 (2002).

12. T. Tokushima, *et al.*, *Chemical Physics Letters* **460**, 387 (2008).

13. O. Fuchs, *et al.*, *Physical review letters* **100**, 027801 (2008).

14. G. Sansone, *et al.*, *Nature* **465**, 763 (2010).

15. S. Biswas, *et al.*, *Nat. Phys.* **16**, 778-783 (2020).

16. P. M. Kraus, *et al.*, *Science* **350**, 790 (2015).

17. M. Huppert, I. Jordan, D. Baykusheva, A. von Conta, H. J. Wörner, *Phys. Rev. Lett.* **117** (2016).

18. M. Schultze, *et al.*, *Science* **328**, 1658 (2010).

19. K. Klünder, *et al.*, *Phys. Rev. Lett.* **106**, 143002 (2011).

20. V. Loriot, *et al.*, *J. Phys. Photonics* **2**, 024003 (2018).

21. J. M. Dahlström, A. L'Huillier, A. Maquet, *Journal of Physics B: Atomic, Molecular and Optical Physics* **45**, 183001 (2012).

22. R. Pazourek, S. Nagele, J. Burgdörfer, *Rev. Mod. Phys.* **87**, 765 (2015).

23. D. Baykusheva, H. J. Wörner, *The Journal of Chemical Physics* **146**, 124306 (2017).

24. A. L. Cavalieri, *et al.*, *Nature* **449**, 1029 (2007).

25. S. Neppl, *et al.*, *Nature* **517**, 342 (2015).

26. M. Ossiander, *et al.*, *Nature* **561**, 374 (2018).

27. R. Locher, *et al.*, *Optica* **2**, 405 (2015).

28. Z. Tao, *et al.*, *Science* **353**, 62 (2016).

29. F. Siek, *et al.*, *Science* **357**, 1274 (2017).

30. L. Seiffert, *et al.*, *Nature Physics* **13**, 766 (2017).

31. M. Isinger, *et al.*, *Science* **358**, 893 (2017).

32. V. Gruson, *et al.*, *Science* **354**, 734 (2016).

33. I. Jordan, H. J. Wörner, *Journal of Optics* **20**, 024013 (2018).

34. I. Jordan, M. Huppert, M. A. Brown, J. A. van Bokhoven, H. J. Wörner, *Review of Scientific Instruments* **86**, 123905 (2015).

35. A. von Conta, M. Huppert, H. J. Wörner, *Review of Scientific Instruments* **87** (2016).

36. D. Rattenbacher, I. Jordan, A. Schild, H. J. Wörner, *Physical Review A* **97**, 063415 (2018).

37. H. Shinotsuka, *et al.*, *Surface and Interface Analysis* **49**, 238 (2017).

38. A. Schild, M. Peper, C. Perry, D. Rattenbacher, H. J. Wörner, *J. Phys. Chem. Lett.* **11**, 1128 (2020).

39. S. Thürmer, *et al.*, *Nature Chemistry* **5**, 590 (2013).

40. Y.-I. Suzuki, K. Nishizawa, N. Kurahashi, T. Suzuki, *Phys. Rev. E* **90**, 010302 (2014).

41. T. Jahnke, *et al.*, *Nature Physics* **6**, 139 (2010).

42. M. Mucke, *et al.*, *Nature Physics* **6**, 143 (2010).

43. I. Unger, *et al.*, *Nature chemistry* **9**, 708 (2017).

44. I. Jordan, *et al.*, Data for "Attosecond Spectroscopy of Liquid Water", Zenodo repository. DOI: 10.5281/zenodo.3934437

45. M. Huppert, I. Jordan, H. J. Wörner, *Review of Scientific Instruments* **86**, 123106 (2015).

46. J. Chambers, W. Cleveland, B. Kleiner, P. Tukey, *Graphical Methods for Data Analysis* (Wadsworth, Bellmont, 1983).

47. C. Peltz, C. Varin, T. Brabec, T. Fennel, *Computational strong-field quantum dynamics* (De Gruyter, 2017), chap. Microscopic particle-in-cell approach.

48. Lumerical, Lumerical solutions, inc., `http://www.lumerical.com/tcad-products/fdtd/`.

49. G. M. Hale, M. R. Querry, *Appl Opt* **12**, 555 (1973).

50. Refractive index database, `http://https://refractiveindex.info`.

51. N. M. Kroll, K. M. Watson, *Phys. Rev. A* **8**, 804 (1973).

52. L. B. Madsen, *Am. J. Phys.* **73**, 57 (2005).

53. Álvaro Jiménez Galán and Luca Argenti and Fernando Martín, *New Journal of Physics* **15**, 113009 (2013).

54. K. L. Reid, *Annu. Rev. Phys. Chem.* **54**, 397 (2003).

55. J. Tennyson, *et al.*, *Journal of Physics: Conference Series* **86**, 012001 (2007).

56. B. Temelso, K. A. Archer, G. C. Shields, *The Journal of Physical Chemistry A* **115**, 12034 (2011). PMID: 21910428.

57. A. P. P. Natalense, R. R. Lucchese, *J. Chem. Phys.* **111**, 5344 (1999).

58. F. A. Gianturco, R. R. Lucchese, N. Sanna, *J. Chem. Phys.* **100**, 6464 (1994).

Supplementary Materials for Attosecond spectroscopy of liquid water

Inga Jordan, Martin Huppert[†], Dominik Rattenbacher[‡], Michael Peper, Denis Jelovina, Conaill Perry, Aaron von Conta, Axel Schild, and Hans Jakob Wörner[*]

Laboratorium für Physikalische Chemie, ETH Zürich, Zurich, Switzerland

[*]Corresponding authors: hwoerner@ethz.ch; www.atto.ethz.ch.

[†]Present address: Paul Scherrer Institut, CH-5232 Villigen PSI, Switzerland

[‡]Present address: Max Planck Institute for the Science of Light, Staudtstr. 2, D-91058 Erlangen, Germany

This pdf file includes:

Contents

1 Experimental Setup

The experimental setup consists of an actively-stabilized attosecond beamline (45) and a photoelectron spectrometer equipped with a liquid microjet (34). The APT is created by high-harmonic generation of a $\sim$1.5-mJ, 30-fs laser pulse centered at 800 nm in a gas cell filled with $\sim$20 mbar argon. The APT is subsequently separated from the driving IR field using a mirror with a center hole, transmitted through a 100μm-thin metal foil (Ti or Sn), and recombined with the attenuated IR field. The optical-path length difference of the APT and the IR field is scanned with a piezo-electric stage and actively stabilized to $\sim$20-as accuracy using combined white-light and monochromatic-laser interferometers (for details, see (45)). The 800-nm laser source used in these experiments was not carrier-envelope phase (CEP) stabilized. CEP stabilization is not necessary because the time-delay information is extracted from the phase shift between the simultaneously recorded side-band signals, which does not depend on the CEP. Liquid water is delivered into the interaction region of the magnetic-bottle photoelectron spectrometer through a cylindrical quartz nozzle with an inner diameter of 25 μm using a high-pressure liquid-chromatography pump. NaCl is added to the water at a concentration of 50 mmol/L to suppress electrokinetic charging and the jet is electrically grounded. A conically shaped permanent magnet guides the photoelectrons into a 1-m long drift tube equipped with a solenoid. The photoelectrons are detected by a microchannel-plate detector with a sub-ns response time. The energy resolution of the spectrometer is 0.16-0.34 eV over the energy range studied here (34).

2 Data processing

The data processing is based on first interpolating the raw data onto an equidistant kinetic-energy grid, then identifying spectral contributions from gas- and liquid-phase water for all harmonic and sideband orders by fitting the delay-integrated spectra and finally extracting the phases of their oscillations. These steps are explained in more detail in the following.

2.1 Conversion

The analysis of attosecond-interferometry scans starts with the conversion of the time-of-flight axis to a kinetic-energy axis. The experimental data are subsequently interpolated to an equidis-

tant kinetic-energy grid. The Jacobi correction and the energy-dependent collection efficiency of the spectrometer compensate each other in the kinetic-energy range above ∼5 eV. This is verified by the electron counts being consistent with literature cross sections.

2.2 Fitting of delay-integrated spectra

The XUV-only spectrum was fitted using principal-component spectra for liquid- and gas-phase water from a monochromatized high-harmonic radiation source (35). One single principal component represents the gas- or the liquid-phase water photoelectron spectrum generated with XUV radiation consisting of only one harmonic order. An overview of the measured principal components and the corresponding fits is shown in Figure S1.

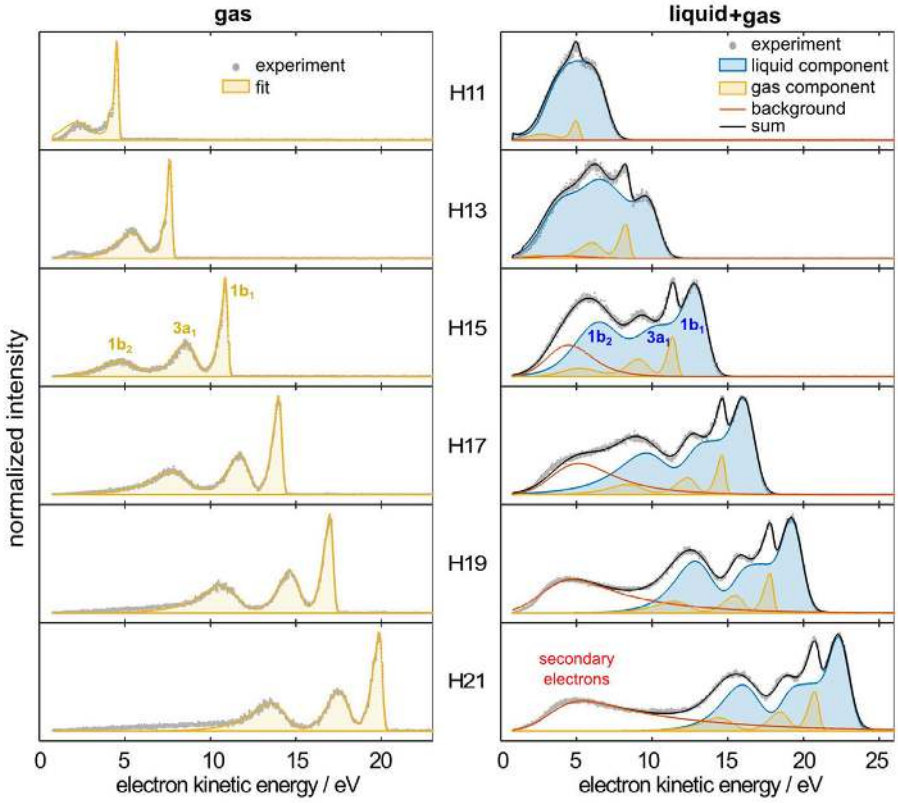

Figure S1: **Experimental single-harmonic spectra of gas-phase and liquid water generated using odd harmonic orders 11-21 from a monochromatic high-harmonic radiation source and their fits.** The left panel shows the pure gas-phase photoelectron spectra obtained by moving the jet out of the XUV focus. The panel on the right-hand side shows the photoelectron spectra recorded with the jet in the XUV focus. Each filled curve corresponds to one principal component used in the complex-valued fitting approach.

In a first step, the XUV-only spectrum containing liquid- and gas-phase contributions generated with three dominant harmonic orders (odd orders 17-21 in the case of the Ti filter, odd orders 11-15 in the case of the Sn filter) was fitted. The individual principal components were shifted along the kinetic-energy axis in order to account for day-to-day variations of the harmonic frequency, convoluted with a Gaussian and scaled in intensity. The results obtained from the fit are presented in Fig. S2a (and Fig. 2a of the main text).

In a second step sideband components were generated by shifting each principal component by one IR photon energy (1.55 eV) to higher kinetic energies, intensity scaling and adding it to the XUV-only spectrum. Fitting the XUV+IR experimental spectrum is then performed by scaling the single-components from the XUV-only spectrum and the sideband components. Additionally the sideband components were also allowed to shift slightly in energy. The corresponding fit is shown in Fig. S2b (and Figure 2a of the main text).

Finally, the difference spectrum generated by subtracting the delay-integrated XUV+IR spectrum from the delay-integrated XUV-only spectrum was fitted as well using the components retrieved from the fit of the XUV+IR spectrum. The advantage of the difference spectrum is the much higher energy sensitivity and the straightforward assignment of spectral regions dominated by the main photoelectron bands (negative contributions) and the sidebands (positive contributions). The corresponding fits are shown in Fig. S2c (and Fig. 2b of the main text).

2.3 Phase extraction

The last step consists in extracting the phase shifts between the oscillations of the liquid- and gas-phase sideband spectra. For this purpose, the measured difference spectra (Fig. S3a) are Fourier-transformed along the XUV-IR time-delay axis. The obtained complex-valued Fourier transform, shown in Fig. S3b in terms of its power spectrum, is then itself subjected to the principal-component analysis, which yields the desired phase shifts. The details of this procedure have been described in Ref. (33).

Briefly, the complex-valued Fourier transform, shown in Figs. S3c and d is subjected to a non-linear fit that keeps the amplitudes of the principal components fixed to their values obtained

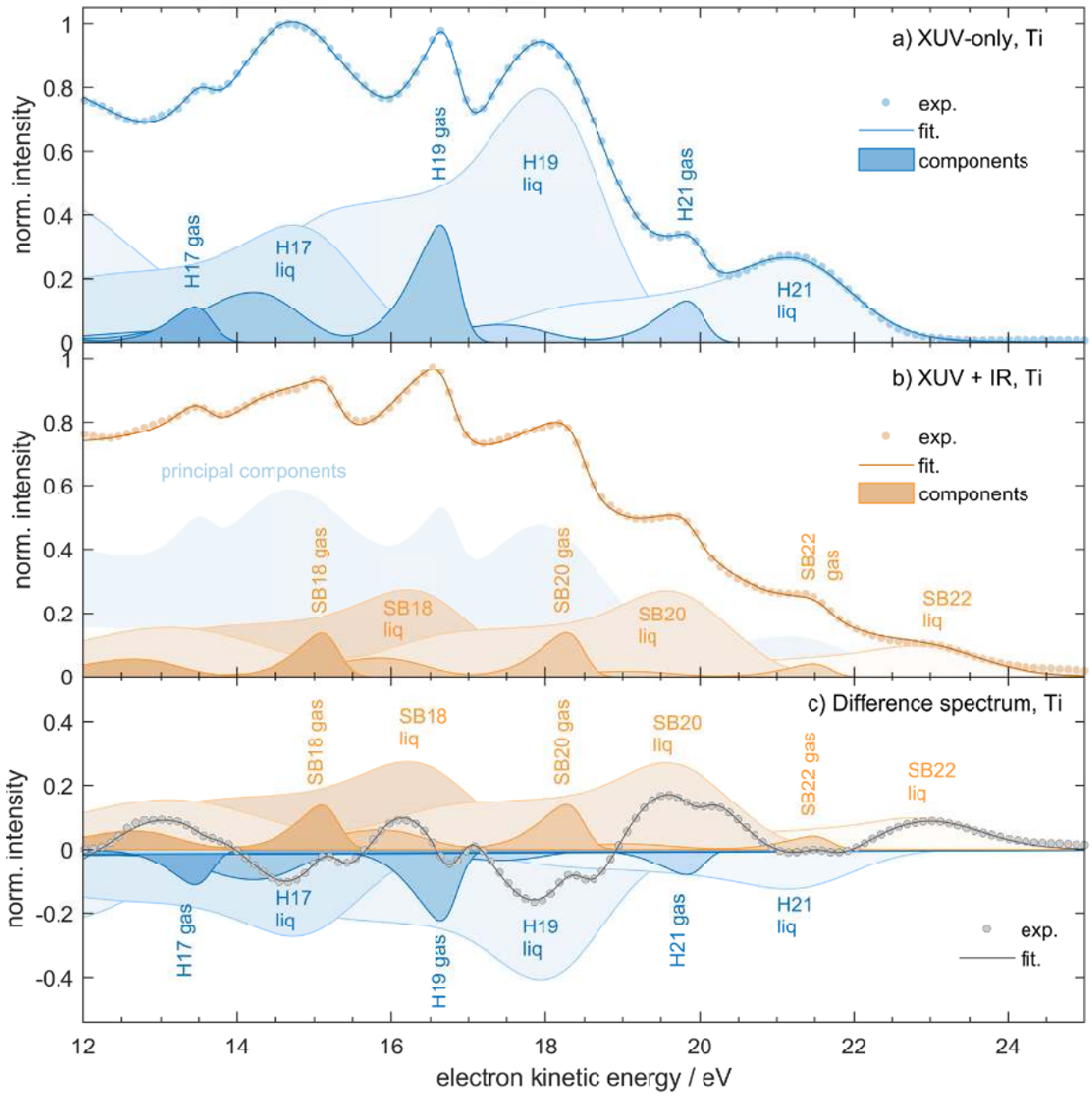

Figure S2: **Illustration of the fitting procedure of XUV-only, XUV+IR and difference photoelectron spectra.** Circles represent data points, the solid lines account for the fit and the filled curves indicate the single-harmonic spectra. Gas- and liquid-phase water contributions are labelled in the graphs. Exemplary fits are shown for delay-integrated a) XUV-only spectrum, b) XUV+IR spectrum and c) the difference spectrum.

from the delay-integrated difference spectra, but multiplies each amplitude with a complex value e^z, where $z = \Re(z) + \mathrm{i}\Im(z)$ is the fitting parameter. The principal components weighted by these complex coefficients are then added together and fitted to the complex-valued Fourier transform. The successful retrieval of the phase information contained in the Fourier transform

is visible in the perfect agreement between the data points and the fitted line over the entire range of interest (Figs. S3c and d).

The complex number assigned to each principal component carries the information about the phase shift of the corresponding oscillation, encoded in $\Im(z)$, whereas the oscillating fraction of the component's intensity is given by $\mathrm{e}^{\Re(z)}$. In this way, our analysis allows for a finite modulation contrast, which was required to properly fit the measured data. The physical origin of this finite modulation contrast is discussed in the main text. The oscillation amplitude of a given principal component contributing to the Fourier transform is then given by $A\mathrm{e}^{\Re(z)}$, where A is the amplitude of each principal component retrieved from fitting the delay-integrated spectra (see section 2.2). In this way, the contribution of each oscillating component is fully characterized in terms of its modulation contrast and its phase shift. An overview of these results is given in Figure S3. Single-harmonic components present in the region of interest (17-21 eV) are gas-phase sideband order 20, liquid-phase sideband order 20 and gas-phase principal peak associated with harmonic order 21. The associated photoelectron peaks are dominated by ionization from the $1b_1$ band, however, the $3a_1$ of the liquid component also plays a role in this region. The phase is assumed to the constant over the entire single-harmonic spectrum, which in the case of the gas-phase component is a valid approximation in the kinetic-energy region under investigation (17). For the liquid component this assumption gave satisfying agreement between fit and experimental data, which validates the assumption.

The relative modulation depth M_{rel} between the liquid- and gas-phase sideband peaks, reported in the main text, can be directly inferred from the oscillating fractions of the peak amplitudes

$$M_{\mathrm{rel}} = \frac{\mathrm{e}^{\Re(z_{\mathrm{liq}})}}{\mathrm{e}^{\Re(z_{\mathrm{gas}})}}. \tag{1}$$

3 Delay statistics

Phases extracted from attosecond-interferometry scans are presented as histograms in Figure S4. In the case of sideband order 14 a total of 13 scans were considered for the evaluation, in the case of sideband order 20 a total of 27 scans. Gaussian distributions with mean values and standard deviations determined from the distribution of experimental values are shown as a guide to the eye in Figure S4 as solid lines.

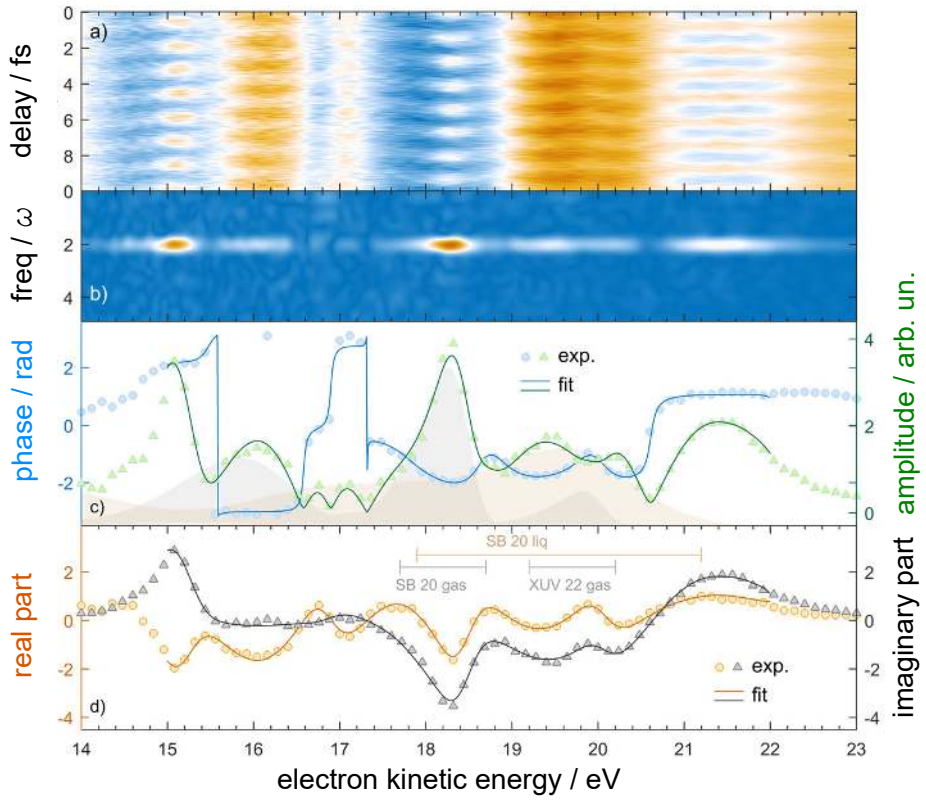

Figure S3: **Exemplary determination of oscillation phases.** a) shows the experimental RABBIT trace in the form of difference spectra. b) shows the power spectrum of the Fourier-transformed spectrogram in a). Integrating within the boundaries of the 2ω-oscillation of the Fourier transform gives a complex-valued array whose phase and magnitude are shown in c). The phase data refers to the left axis and the amplitude to the right axis. Panel d) shows the real and the imaginary parts of the complex-valued Fourier transform. Experimental data points are shown as symbols in c) and d), whereas the result of the complex fit is represented as solid line.

A normal probability plot (46) was generated with the normplot function implemented in Matlab in order to judge how well the experimental data resemble normal behavior. The results are presented in Figure S5, where the straight line indicates the reference for a normally distributed sample. For both sideband orders, the experimental data points nicely resemble the linear behavior in the normal distribution plot. These results imply that the experimental values can be considered as normally distributed. The mean values, standard deviations and 95% confidence intervals are summarized in Table S1.

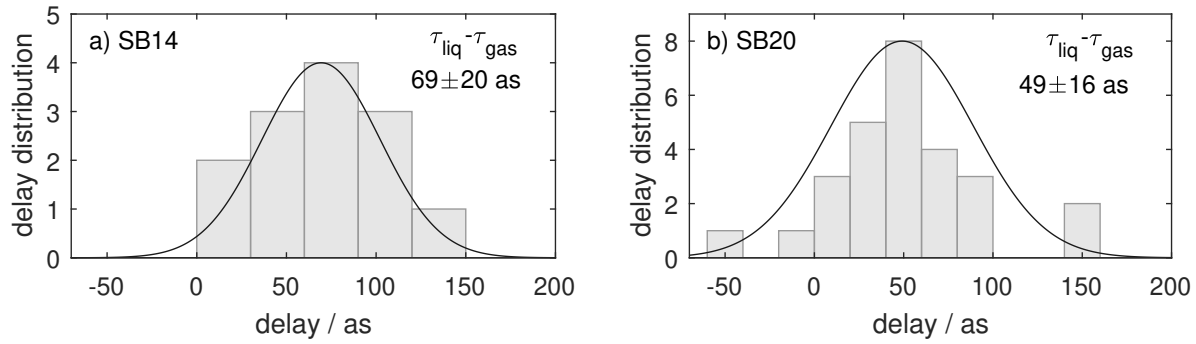

Figure S4: **Distributions of photoionization delays between liquid and gas-phase water** ($\tau_{\mathrm{liq}} - \tau_{\mathrm{gas}}$) for a) sideband order 14 obtained from $N = 13$ RABBIT scans using a Sn filter and b) sideband order 20 obtained from $N = 27$ RABBIT scans using a Ti filter. XUV and IR radiation were p-polarized. Solid lines indicate Gaussian functions with positions (mean delays), widths (standard deviation, normalized by $N - 1$) and scaled in amplitude according to the experimental data. The indicated errors correspond to the 95% confidence intervals.

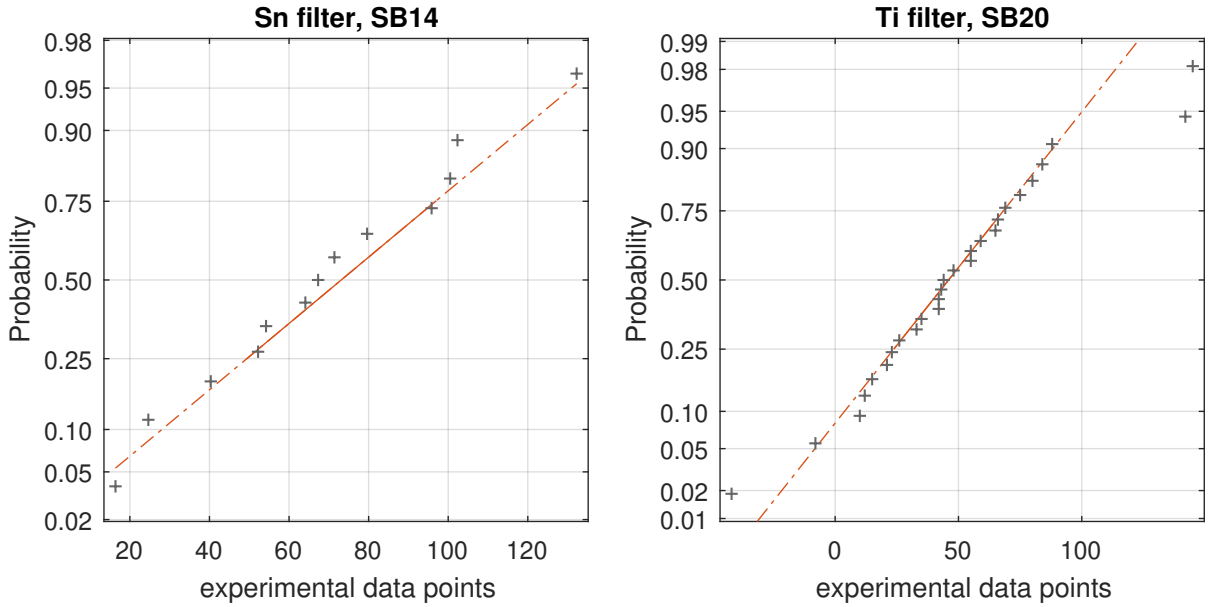

Figure S5: **Normal probability plots for a) sideband order 14 and b) sideband order 20.** The red line indicates a normally distributed sample, the crosses represent data points. Systematic deviations from the linear behavior of the normal sample indicate departures from normality.

	mean delay / as	number of scans	standard deviation / as	95% confidence interval / as
SB14	69	13	33	20
SB20	49	27	40	16

Table S1: **Statistics of the phases retrieved from experimental RABBIT scans using Sn and Ti filters.**

4 Near-field distributions

In this section, we study the influence of the near-field distribution of the XUV and IR fields within and around the liquid jet on the measured delays. These near-field distributions may contribute a non-trivial phase shift to the observed side-band oscillations, which might erroneously be interpreted as a delay, and must therefore be carefully examined. In what follows, we refer to these contributions as "geometric delays". Geometric delays were determined from numerical calculations based on Mie theory. Details can be found in Ref. (47). The calculation requires the energy-dependent relative permittivities ϵ_i of the medium. The permittivities were extracted from Lumerical, a commercial-grade simulator based on the finite-difference time-domain method (48), Ref. (49) and the refractive index data base (50) and are summarized in Table S2. Representative real parts of the near-field distributions are shown in Figure S6 for the infrared

	λ / nm	ϵ_1	ϵ_2	n_r	k
IR	800.00	1.7662	$3.32 \cdot 10^{-7}$	1.329	$1.25 \cdot 10^{-7}$
H13	61.54	0.5019	0.7510	0.8382	0.4480
H15	53.33	0.5915	0.5416	0.8347	0.3244

Table S2: **Permittivities $\epsilon = \epsilon_1 + \mathrm{i}\epsilon_2$ and refractive indices $n = n_r + \mathrm{i}k$ entering the numerical near-field calculations.**

(800 nm) radiation and in Figure S7 for XUV radiation (harmonic order 13) for a jet with a 5 μm diameter. XUV and infrared radiation are both propagating along x and have an initial polarization component along y. The jet cylinder axis is parallel to z. The images thus show the cross section of the liquid jet indicated by white circles.

Relative propagation phases at each point of the grid can be directly computed from the near-field distributions according to

$$\mathbf{k}_{\mathrm{xuv}}^{q+1} \cdot \mathbf{r} - \mathbf{k}_{\mathrm{xuv}}^{q-1} \cdot \mathbf{r} - 2\mathbf{k}_{\mathrm{ir}} \cdot \mathbf{r} = \arg(\mathcal{E}_{\mathrm{xuv}}^{q+1}) - \arg(\mathcal{E}_{\mathrm{xuv}}^{q-1}) - 2\arg(\mathcal{E}_{\mathrm{ir}}) \tag{2}$$

and are visualized in Figure S8. Here, $\mathcal{E}$ is the complex-valued output electric field of the near-field calculation, $\mathbf{k}$ is the wave vector and $\mathbf{r}$ is the distance. Thus, $\mathbf{k} \cdot \mathbf{r}$ is the propagation phase of the corresponding field.

In order to retrieve the total geometric delays for the entire gas- and the liquid-phase, the relative

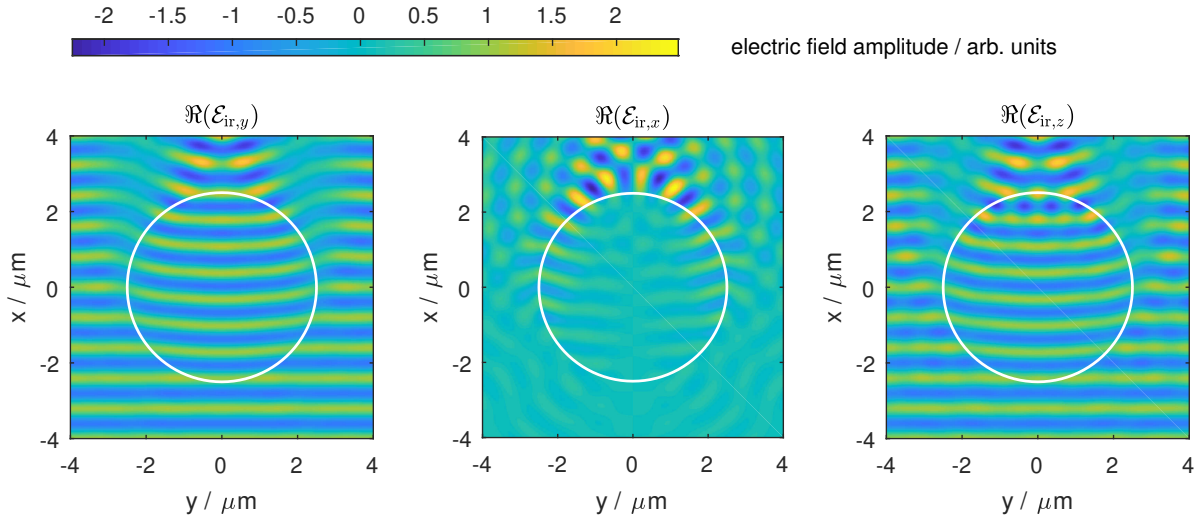

Figure S6: **Near-field distributions of the electric-field amplitude (real part of the electric field as obtained from the Mie-solver) of the infrared radiation propagating along x for polarization components along y (left), x (middle) and z (right).** The cross section of the jet (5 μm diameter) is indicated by the white circle, its cylindrical axis is along z.

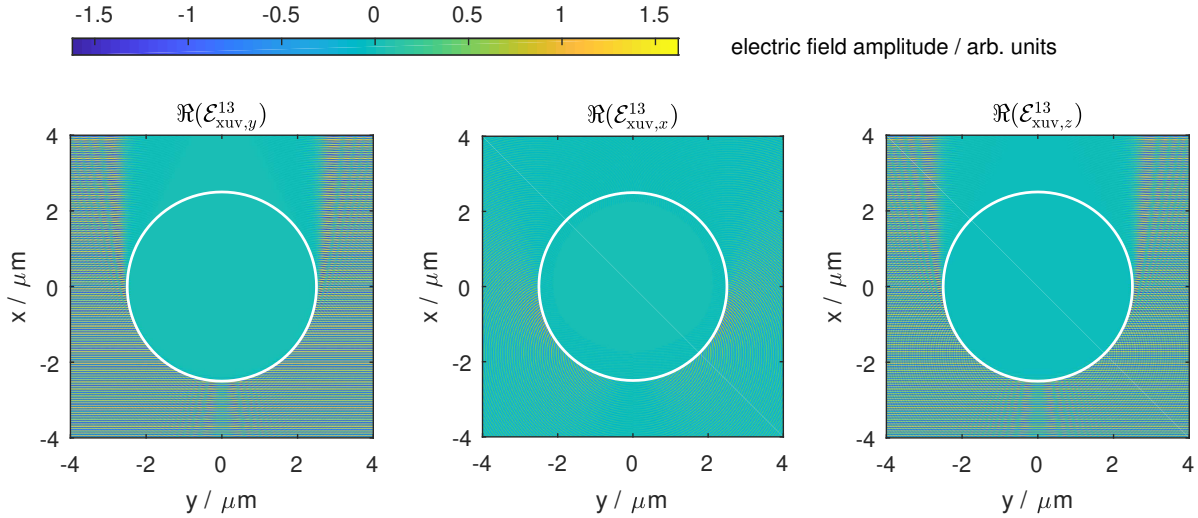

Figure S7: **Near-field distributions of the electric field amplitude (real part of the electric field as obtained from the Mie-solver) of the XUV radiation (harmonic order 13) propagating along x for polarization components along y (left), x (middle) and z (right).** The cross section of the jet (5 μm diameter) is indicated by the white circle, its cylindrical axis is along z.

propagation phases at each grid point have to be properly combined. An analytical expression was derived based on the result of the second-order perturbation theory as follows. Considering

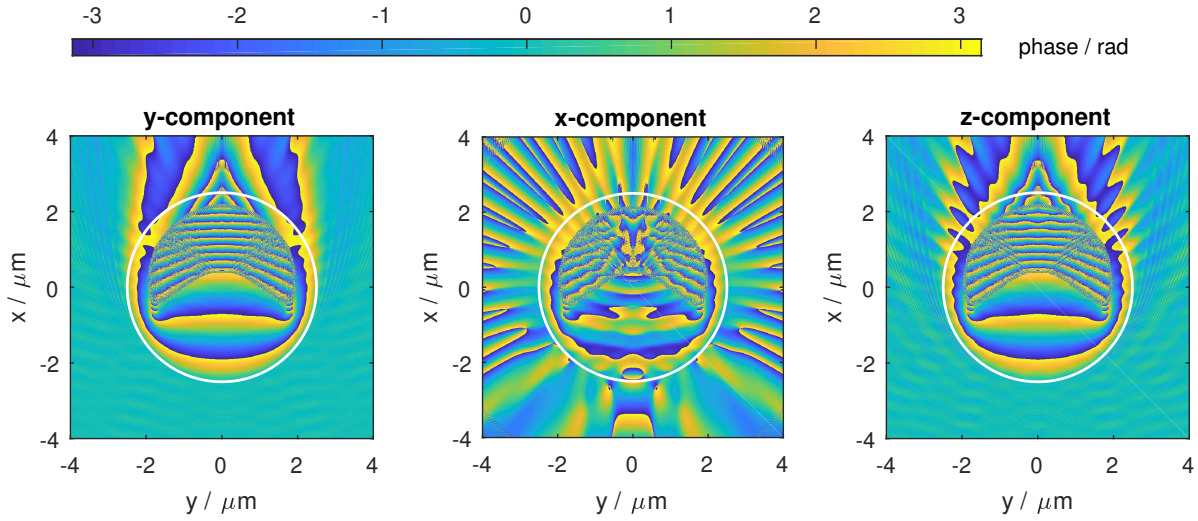

Figure S8: **Relative propagation phases according to** $(\mathbf{k}_{\mathrm{xuv}}^{q+1} - \mathbf{k}_{\mathrm{xuv}}^{q-1} - 2\mathbf{k}_{\mathrm{ir}}) \cdot \mathbf{r} = \arg(\mathcal{E}_{\mathrm{xuv}}^{q+1} - \mathcal{E}_{\mathrm{xuv}}^{q-1} - 2\mathcal{E}_{\mathrm{ir}})$ **at each point of the grid for all three polarization components.** The cross section of the jet (5 μm diameter) is indicated by the white circle, its cylindrical axis is along z.

only geometric contributions ($\delta_{xuv}^{q} = 0$) the quantum path interference reads

$$c_q(\mathbf{r}) = \left|\mathcal{E}_{\mathrm{xuv}}^{q-1}(\mathbf{r})\right| \left|\mathcal{E}_{\mathrm{ir}}(\mathbf{r})\right| e^{\mathrm{i}\mathbf{k}_{\mathrm{xuv}}^{q-1}\cdot\mathbf{r}} e^{\mathrm{i}(\delta_{\mathrm{ir}}+\mathbf{k}_{\mathrm{ir}}\cdot\mathbf{r})} + \left|\mathcal{E}_{\mathrm{xuv}}^{q+1}(\mathbf{r})\right| \left|\mathcal{E}_{\mathrm{ir}}(\mathbf{r})\right| e^{\mathrm{i}\mathbf{k}_{\mathrm{xuv}}^{q+1}\cdot\mathbf{r}} e^{-\mathrm{i}(\delta_{\mathrm{ir}}+\mathbf{k}_{\mathrm{ir}}\cdot\mathbf{r})}. \tag{3}$$

The transition probability is then given by

$$\begin{aligned} |c_q(\mathbf{r})|^2 = 2\underbrace{\left|\mathcal{E}_{\mathrm{xuv}}^{q-1}(\mathbf{r})\right| \left|\mathcal{E}_{\mathrm{xuv}}^{q+1}(\mathbf{r})\right| \left|\mathcal{E}_{\mathrm{ir}}(\mathbf{r})\right|^2}_{A(\mathbf{r})} \cos\left(2\delta - \underbrace{\left(\mathbf{k}_{\mathrm{xuv}}^{q+1} - \mathbf{k}_{\mathrm{xuv}}^{q-1} - 2\mathbf{k}_{\mathrm{ir}}\right)\mathbf{r}}_{\phi(\mathbf{r})}\right) \\ + \underbrace{\left|\mathcal{E}_{\mathrm{xuv}}^{q-1}(\mathbf{r})\right|^2 \left|\mathcal{E}_{\mathrm{ir}}(\mathbf{r})\right|^2 + \left|\mathcal{E}_{\mathrm{xuv}}^{q+1}(\mathbf{r})\right|^2 \left|\mathcal{E}_{\mathrm{ir}}(\mathbf{r})\right|^2}_{B(\mathbf{r})}. \end{aligned} \tag{4}$$

Assuming that the contributions from electrons originating from different generation points can be added incoherently, the total transition probability as a function of the XUV-IR delay δ is obtained from the following summation over all near-field coordinates (x, y)

$$\sum_{x,y} |c_{x,y} \cdot w(x,y)|^2 = \sum_{x,y} \Big[2A(x,y)\cos(2\delta_{\mathrm{ir}} - \phi(x,y)) + B(x,y)\Big] \cdot w(x,y) \tag{5}$$

where $w(x, y)$ is a weighting factor. For gas-phase regions of the near-field distribution, i.e. where the distance $d = \sqrt{x^2 + y^2}$ to the center point is larger than the liquid-jet radius R, the weighting factor takes into account the radially decreasing gas density,

$$w(x,y) \propto \frac{1}{d(x,y) - R}. \tag{6}$$

For the liquid-phase regions, where $d \leq R$, the weighting factor reflects the electron-signal attenuation as a function of the probe depth (in terms of the effective attenuation length, EAL) according to

$$w(x,y) \propto \exp\left(-\frac{R - d(x,y)}{\mathrm{EAL}}\right). \tag{7}$$

Polarization components along x and y were combined in order to account for a total delay associated with a p-polarized laser radiation, whereas the polarization component along z accounts for s-polarized laser radiation. The summation of cosine functions with varying amplitudes can be reformulated based on a trigonometric identity such that

$$\sum_{x,y} |c_{x,y} \cdot w(x,y)|^2 = 2A' \cos\left(2\delta_{\mathrm{ir}} - \phi_{\mathrm{geom}}\right) + \sum_{x,y} B(x,y) \cdot w(x,y) \tag{8}$$

where

$$\begin{aligned} A' &= \sqrt{\sum_{x,y,v,w} A(x,y)A(v,w)\cos\left(\phi(x,y) - \phi(v,w)\right)} \\ &= \sqrt{\left[\sum_{x,y} A(x,y)\cos(x,y)\right]^2 + \left[\sum_{x,y} A(x,y)\sin(x,y)\right]^2} \end{aligned} \tag{9}$$

and

$$\phi_{\mathrm{geom}} = \mathrm{atan2}\left(\sum_{x,y} A(x,y)\sin(\phi(x,y)), \sum_{x,y} A(x,y)\cos(\phi(x,y))\right). \tag{10}$$

Thus, the total geometric delay is directly extracted from the near-field distributions after matrix multiplication, summation and employing the atan2 function. The modulation depth M is available as well from the amplitude A' and the non-oscillating summands in equation 8 based on the following relation

$$M = \frac{A'}{\sum_{x,y} B(x,y) \cdot w(x,y)}. \tag{11}$$

The results for both gas- and liquid-phase geometric delays as well as their relative delay for various jet diameters are shown in Figure S9. The EAL was chosen to be 2 nm, in agreement with Ref. (40).

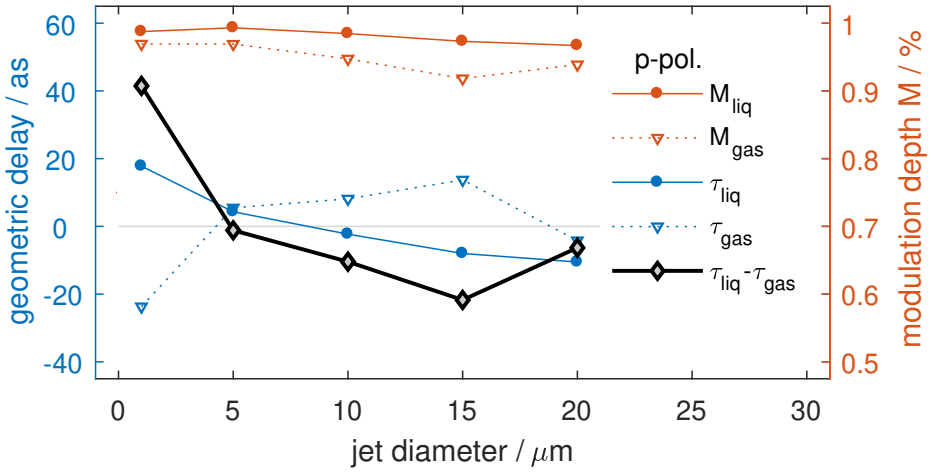

Figure S9: **Geometric delays (blue) and corresponding modulation depths (red) as a function of the jet diameter.** The relative delay of liquid water with respect to gas-phase water is shown as gray-filled diamonds.

5 Monte-Carlo Trajectory Simulations

We use Monte-Carlo trajectory simulations to estimate the contribution of electron scattering during transport on the measured delays. During each collision, the system may absorb or emit an IR photon, thereby changing the photoelectron kinetic energy (eKE). These processes induce an additional ("non-local") delay τ_{nl} that adds to the ("local") photoionization delay τ^{P}, i.e., the measured delay is (36)

$$\tau = \tau^{\mathrm{P}} + \tau_{\mathrm{nl}}. \tag{12}$$

We have previously investigated the behavior of τ_{nl} for a one-dimensional model and have found that the results of the time-dependent Schrödinger equation can be reproduced with a semi-classical trajectory-based model that includes photoionization, electron scattering, their laser-assisted counterparts, as well as all relevant phases (36). Based on this physical insight, a 3D trajectory continuum model for the simulation of attosecond interferometry of liquid water was developed to interpret the experimental results.

The model works as follows:

- **Ionization:** An ionization depth $z < 0$ is chosen randomly, from which a set of trajectories is launched. Each trajectory is described by a polar angle θ with respect to the

common XUV and IR polarization axis, chosen randomly from the probability distribution $|f^{\mathrm{LAPE}}_{m+n,m}(\theta)|^2$ (defined below), and an azimuthal angle chosen randomly from a uniform probability distribution. Each trajectory is randomly given a maximum path to travel according to the probability distribution function

$$P(r) = \frac{1}{r_{\mathrm{c}}} e^{-r/r_{\mathrm{c}}} \tag{13}$$

with r_{c} = IMFP being the inelastic mean free path, i.e., the distance at which inelastic scattering occurs such that the photoelectron loses enough energy to not be detected within the relevant eKE range, i.e. the sideband width.

- **Scattering:** For each trajectory, a distance is randomly drawn according to Eq. (13) with r_{c} = EMFP being the elastic mean free path, and the positions of the trajectories are updated. At this distance, elastic scattering is assumed to be happening, and the scattering angles are drawn randomly from the distribution $|f^{\mathrm{LAES}}_{m+n,m}(\theta,\phi)|^2$ (defined below).

  The procedure to simulate elastic collisions is repeated until the total path traveled by a trajectory is longer than its initially set maximum path (then inelastic scattering is assumed to happen and the trajectory is discarded) or until it reaches the water surface at $z = 0$ (then the trajectory is detected if its polar angle relative to the z-axis is smaller than the selected detector acceptance angle).

- **Interaction with the IR field:** Each trajectory is in a state $q-1$, q, or $q+1$, corresponding to an eKE of $(q-1)\omega - E_{\mathrm{b}}$, $q\omega - E_{\mathrm{b}}$, and $(q+1)\omega - E_{\mathrm{b}}$, respectively, where E_{b} is the electron binding energy of liquid water and ω is the frequency of the assisting IR laser field. q is an even number. Half of the trajectories start in state $q-1$ and half in state $q+1$, which simulates ionization with the XUV pulse that was produced by high-harmonic generation with the help of the IR field (and that contains only frequencies that are odd multiples of ω). Due to interaction with the assisting laser field, the system can absorb or emit IR photons during ionization and scattering, and can in this way reach state q.

  IR-field-dressed photoionization amplitudes $f^{\mathrm{LAPE}}_{m+n,m}(\theta)$ (where LAPE stands for laser-assisted photoelectric effect) and scattering amplitudes $f^{\mathrm{LAES}}_{m+n,m}(\theta,\phi)$ (where LAES stands for laser-assisted electron scattering) are obtained from the field-free counterparts $f^{\mathrm{PE}}_{m+n}(\theta)$

and $f^{\mathrm{ES}}_{m+n}(\theta)$, respectively, within the soft-photon approximation (51–53). This procedure was previously detailed in the one-dimensional case in Ref. (36). Here, we provide the relevant formulae for the three-dimensional case. Explicitly,

$$f^{\mathrm{LAPE}}_{m+n,m}(\theta) = f^{\mathrm{PE}}_{m+n}(\theta) e^{in(\pi/2+\omega\Delta t)} J_n\left(\frac{\vec{k}_m \cdot \vec{F}_0}{\omega^2}\right) \tag{14}$$

with wavevector of the ionized electron $\vec{k}_m$, amplitude vector of the IR field $\vec{F}_0 = (0, 0, F_0)$ (polarization directed along the z-axis), with offset Δt between the XUV pulse and the maximum of the IR pulse, and with Bessel function J_n of order n of the first kind. Here, $f^{\mathrm{LAPE}}_{m+n,m}$ represents the amplitude for the transition from state $m+n$ to state m. The present experiments are carried out in a parameter regime where only single-photon transitions are relevant, hence $n = 0, \pm 1$.

Similarly, the laser-dressed scattering amplitude from state $m + n$ to state m is

$$f^{\mathrm{LAES}}_{m+n,m}(\theta, \phi, \theta') = f^{\mathrm{ES}}_{m+n}(\vartheta) e^{in(\pi/2+\omega\Delta t)} J_n\left(\frac{\left(\vec{k}_m - \vec{k}_{m+n}\right) \cdot \vec{F}_0}{\omega^2}\right) \tag{15}$$

with wavevector of the incoming electron $\vec{k}_{m+n}$, wavevector of the outgoing electron $\vec{k}_m$, and with polar scattering angle relative to the incoming electron ϑ. $f^{\mathrm{LAES}}_{m+n,m}$ depends on the polar angle of the incoming direction θ' and the polar and azimuthal angles of the outgoing direction θ, ϕ in the lab frame.

Importantly, and in contrast to previous simulations of attosecond experiments in condensed matter, the trajectories carry a phase. During ionization and scattering, each trajectory can randomly change its state according to the total probabilities for a process determined from the amplitudes $f^{\mathrm{LAPE}}_{m+n,m}$ and $f^{\mathrm{LAES}}_{m+n,m}$, respectively. Then, the phases $\arg f^{\mathrm{LAPE}}_{m+n,m}$ or $\arg f^{\mathrm{LAES}}_{m+n,m}$ are added to the phases of the trajectories. If a trajectory would end in state $q-2$ or $q+2$ after ionization or scattering, it is discarded, because only trajectories ending in sideband q are detected and the probability for changing back to state q if trajectories are in state $q \pm 2$ is negligible.

During propagation to the next position, a phase $k_m r$ is added for the trajectory being in state m and travelling a distance r to the next collision (or to the water surface).

- **Detection:** The second-order amplitude of the detected side-band state is computed as coherent sum over the trajectories that reach the water surface at $z = 0$ in state q, i.e.,

$$c_{q,I}^{(2)}(\Delta t) = \sum_{k=1}^{M_I} e^{i\gamma_k} \tag{16}$$

where M_I is the number of trajectories counted as detected (i.e., escaping the liquid within the detector opening angle) for a given starting depth z_I. Then, the total side-band population is obtained as an incoherent sum over the wavefunctions originating from different starting depths (i.e., for electrons ionized from different positions within the sample),

$$p_q^{(2)}(\Delta t) = \sum_I \frac{M_I}{N_I} |c_{q,I}^{(2)}(\Delta t)|^2, \tag{17}$$

where N_I is the total number of trajectories started at a given initial position z_I. The population $p_q^{(2)}(\Delta t)$ is fitted to a cosine to obtain the delay. Typically, the number of trajectories for a given ionization depth is $N_I \approx 2.5 \times 10^8$. In Fig. S11, the determined delay for a fixed starting depth with ca. this number of trajectories is shown. The accuracy decreases with increasing starting depth because a smaller number of trajectories reach the surface. This is of minor importance for the accuracy that we are aiming at, provided that sufficiently many initial positions are sampled. Figure S10 shows the convergence of the delay with respect to the incoherent average over the ionization depths. Depending on the parameters, about 10^3 runs are necessary to converge the result. We use importance sampling where the ionization depths are chosen according to an exponential distribution e^{z/z_e} (note that $z < 0$) with $z_\mathrm{e} = 5$ nm, because the contributions of trajectories to the final delay decrease with increasing depth $|z|$ due to inelastic scattering.

The field-free photoionization amplitudes $f_m^{\mathrm{PE}}(\theta)$ are obtained from our calculations of small water clusters as mentioned in the main text. We use (54)

$$|f_m^{\mathrm{PE}}(\theta)|^2 \propto 1 + \beta P_2(\cos\theta) \tag{18}$$

with the second-order Legendre polynomial P_2 and asymmetry parameters $\beta = 0.6$ for simulations of sideband $q = 14$ and $\beta = 1.1$ for simulations of sideband $q = 20$. The ionization phase $\arg f_m^{\mathrm{PE}}(\theta)$ was set to zero for all states m, which corresponds to setting the ionization delay τ^{P}

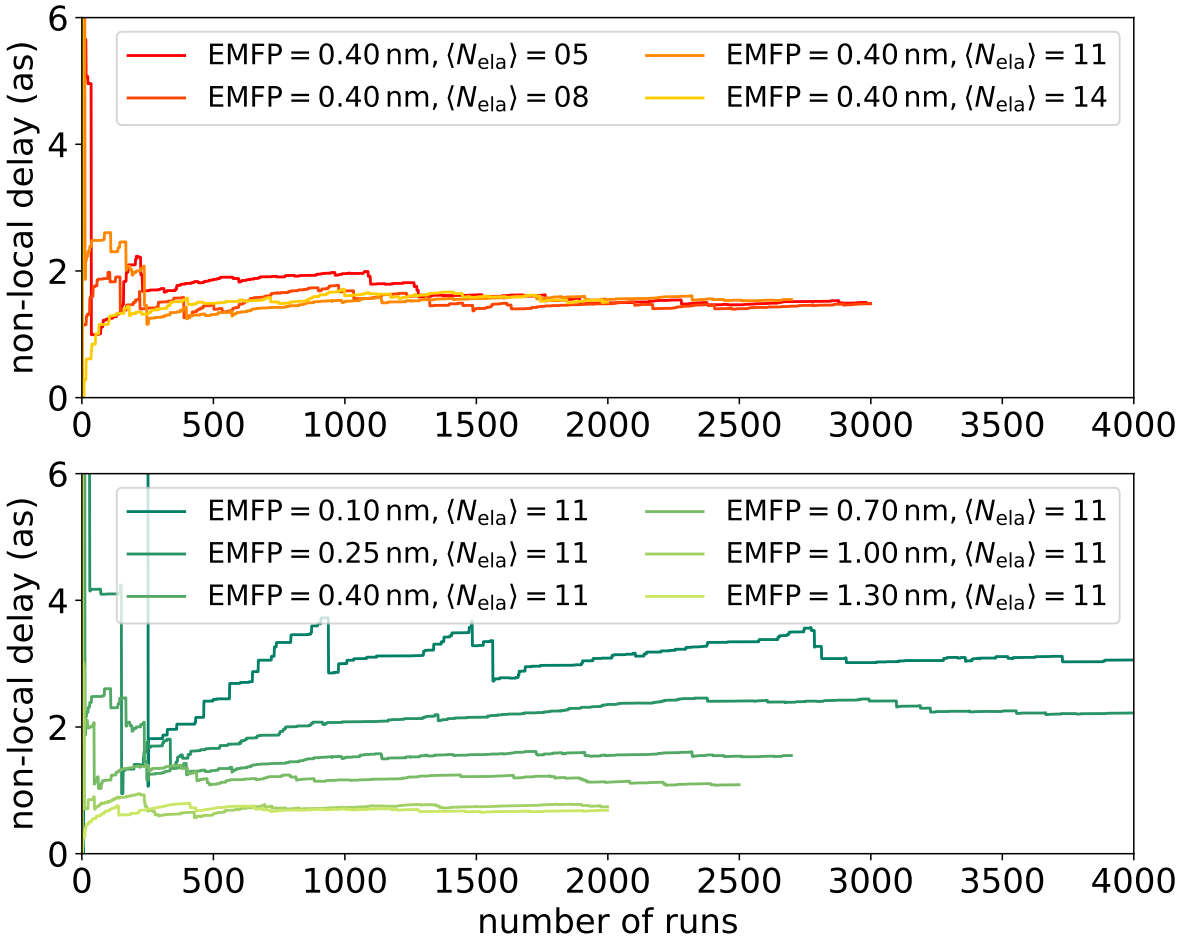

Figure S10: **Convergence of the delay with the number of starting depths that are used in the incoherent average in eqn.** (17)**.** Those starting depths are chosen according to an exponential distribution with a width parameter of 5 nm for all calculations. For the calculation $\mathrm{EMPF} = 0.4\,\mathrm{nm}$, $\langle N_{\mathrm{ela}} \rangle = 11$, for example, we find that starting depths only up to ca. 3 nm have a significant contribution to the final delay.

to zero. Consequently, the trajectory simulation yields only the non-local contribution τ_{nl} to the measured delay.

The field-free scattering amplitudes $f_m^{\mathrm{ES}}(\theta)$ are obtained from calculations of electron scattering at water clusters with the program Quantemol 4.9.5 (55). Quantemol uses the R-matrix method to calculate scattering wavefunctions for electron collisions. We use Hartree-Fock theory and a minimally augmented maug-cc-pVDZ Gaussian-type basis set, because tests with configuration-interaction wave functions and larger basis sets yielded only negligible improvements. The nuclear configurations for the water clusters were chosen to be those obtained from ab-initio calculations (56) with lowest energy. The differential scattering cross sections (DCS) for the monomer compare well with experimental measurements and the DCS also converge rapidly with cluster size, as explained in (38). Hence, we use the calculations for the water heptamer cluster as approximations for scattering in bulk water.

From Quantemol, we obtain both the DCS $|f_m^{\mathrm{ES}}(\vartheta)|^2$ as well as the scattering phases $\arg\left(f_m^{\mathrm{ES}}(\vartheta)\right)$ for eKE corresponding to all relevant states m. The kinetic-energy dependence of the scattering phases is responsible for a scattering delay, which is found to contribute to the non-local delay τ_{nl}. However, our Monte-Carlo calculations show that τ_{nl} is very small in our case, such that the contribution of τ_{nl} is not significant for the results presented in this article.

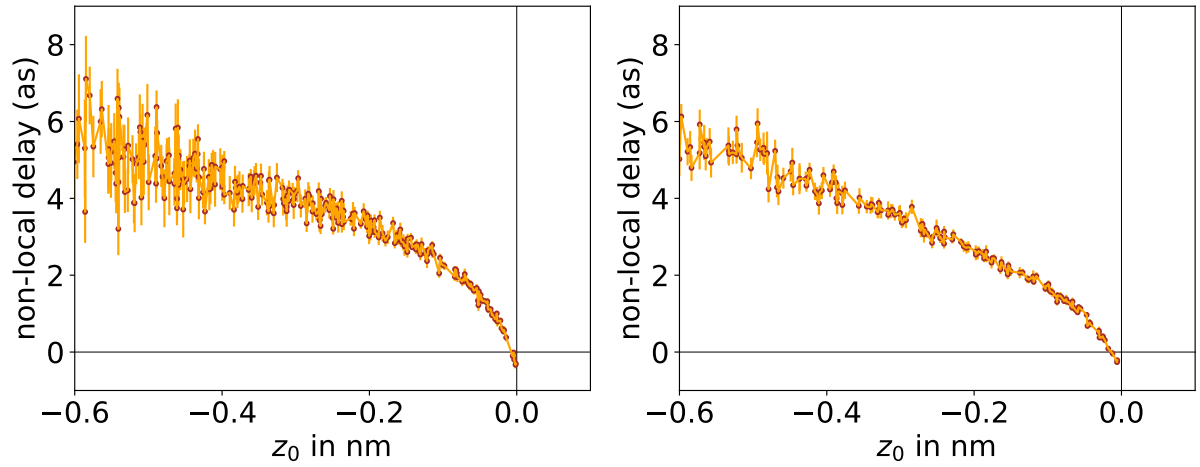

(a) Sideband 14

(b) Sideband 20

Figure S11: **Dependence of the non-local delay on the depth of the ionization site below the surface.**

The values for the elastic and inelastic mean free path, EMFP and IMFP, are determined as described in (38). For the analysis of the calculations, the mean number of elastic scatterings

$$\langle N_{\mathrm{ela}} \rangle = \frac{\mathrm{IMFP}}{\mathrm{EMFP}} \tag{19}$$

is found to be more useful than the IMFP. The default values assumed for the calculations presented here are EMFP = 0.40 nm, $\langle N_{\mathrm{ela}} \rangle = 11$ for sideband $q = 14$, and EMFP = 0.55 nm, $\langle N_{\mathrm{ela}} \rangle = 9$ for sideband $q = 20$. We note that those were preliminary values, with more accurate values determined later as EMFP = 0.56 nm, $\langle N_{\mathrm{ela}} \rangle = 7$ for sideband $q = 14$, and EMFP = 0.84 nm, $\langle N_{\mathrm{ela}} \rangle = 6$ for sideband $q = 20$ (38). However, we did not repeat the expensive calculations because the dependencies of the non-local delay on EMFP and $\langle N_{\mathrm{ela}} \rangle$ presented here illustrate that not much difference is to be expected: If those more accurate values were used, the already negligible estimated contribution of ca. 2 as to the total delay will decrease slightly, e.g. by ca. 0.5 as for sideband 14 (see Figure S10).

Figure S11 shows the dependence of the obtained τ_{nl} on the depth of the ionization site below the water surface for sideband 14 and sideband 20. To obtain this figure, τ_{nl} was determined from $|c^{(2)}_{q,I}(\Delta t)|^2$ from (16) for a given ionization site at depth z_I. While the delay increases with distance from the surface at $z = 0$, the contribution of $p^{(2)}_q(\Delta t)$ to the total delay also decreases due to increasing probability of inelastic scattering that removes the trajectories from the signal, i.e., the factor M_I/N_I in eqn. (17) decreases with the distance from the surface.

In Figure S12, the dependence of the non-local delay τ_{nl} on the EMFP for fixed $\langle N_{\mathrm{ela}} \rangle$ and on $\langle N_{\mathrm{ela}} \rangle$ for fixed EMFP is presented for the case of sideband 14. For fixed $\langle N_{\mathrm{ela}} \rangle$ we observe a behavior similar to what is found in the one-dimensional model of (36), i.e., τ_{nl} decreases with the EMFP. This decrease can be attributed to a combination of the oscillatory dependence of τ_{nl} on the scattering distance (see Fig. 4 of the main text and Ref. (36)) as well as the effect of the averaging over scattering distances.

For fixed EMFP, there is little dependence of τ_{nl} on the average number of scatterings $\langle N_{\mathrm{ela}} \rangle$. From the 1D model of Ref. (36), we expect that for small values of the EMFP, there is an increase of τ_{nl} with $\langle N_{\mathrm{ela}} \rangle$. This is indeed the case, as we verified with complementary calculations where averaging over the distribution of the IMFP was done after the simulation. However,

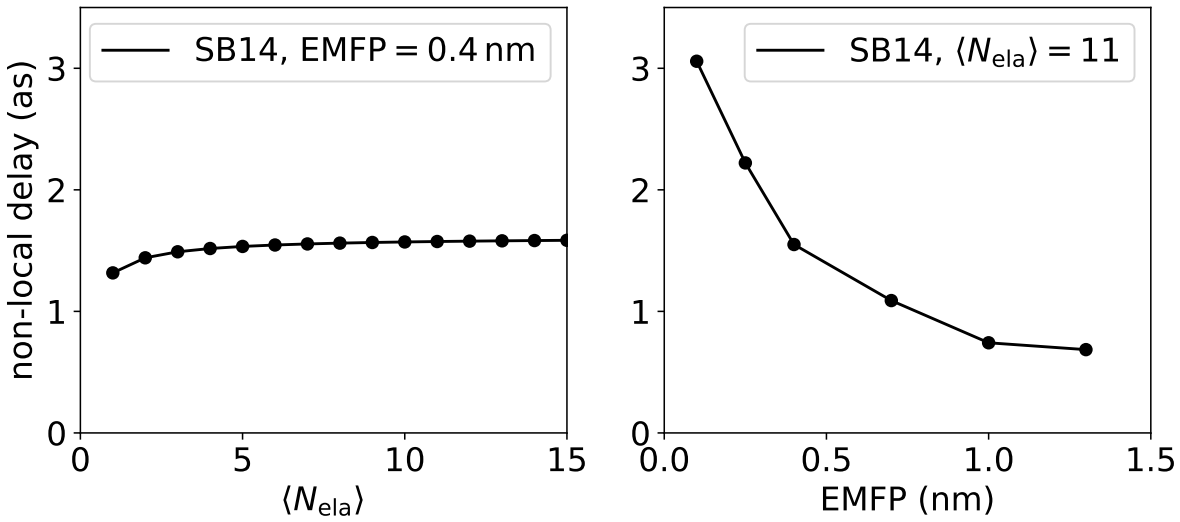

Figure S12: Left: Dependence of the non-local delay on $\langle N_{\mathrm{ela}} \rangle$ for a fixed EMFP = 0.4 nm. Right: Dependence of the non-local delay on the elastic mean free path (EMFP) for a fixed average number of elastic scatterings $\langle N_{\mathrm{ela}} \rangle = 11$.

this increase is small and, for the EMFP of sideband 14, only relevant for $\langle N_{\mathrm{ela}} \rangle < 4$. For larger $\langle N_{\mathrm{ela}} \rangle$, τ_{nl} changes little, as shown in Figure S12. We attribute this to loss of the phase relationship that is needed for τ_{nl} due to scattering in 3D.

This loss of phase relationship is also one of the reasons for the small magnitude of τ_{nl}. Compared to 1D, in the 3D simulations there is the additional effect that trajectories scattering into different angular regions have a different path length to the surface, while in the 1D model the total path length for the added trajectories is always the same. As τ_{nl} relies on certain phase differences, for 3D we expect it to be small if the differential scattering cross section (DCS) is broad. For the considered eKE, the DCS is indeed relatively broad, as shown in (38).

Hence, τ_{nl} may become a more relevant contribution to the total measured delay for higher eKE, when the DCS becomes narrower and when $\langle N_{\mathrm{ela}} \rangle$ is smaller, although there is a competition with the longer EMFP found for higher eKE. Finally, we also note that our trajectory model relies on an asymptotic approximation because each scattering is described by a scattering amplitude that is only valid for an incoming plane wave and an outgoing spherical wave considered at infinite distance. As less coherence can be expected if 3D model potentials with multiple randomly distributed scattering centers are considered, our estimate of the non-local delay can be viewed as an upper bound for the true non-local delay.

6 Calculations of photoionization delays

The photoionization delays have been calculated following the procedure introduced in Ref. (23). The experimental equilibrium geometry of the water molecule has been used. The cluster geometries were constructed on the basis of a tetrahedral coordination geometry with O-O distances of 2.75 Å, corresponding to the first maximum in the pair-correlation function of liquid water. The electronic-structure calculations have been performed using the Gaussian09 program package using the Hartree-Fock method and the cc-pVTZ basis set. The photoionization matrix elements were calculated with the program ePolyScat (57, 58) using an angular-momentum basis up to l_{max}=50 to achieve converged results even for the largest water cluster ($(H_2O)_{11}$). The photoionization delays have been determined from the photoionization matrix elements following the formalism of Ref. (23).